Smart Structures and Systems, *Vol. 30, No. 4 (2022) 353-369*
https://doi.org/10.12989/sss.2022.30.4.353

A new reconfigurable liquid-metal-antenna-based sensor

Xiaoping Zhou*[1], Yihui Fu [1a], Hantao Zhu [1b], Zihao Yu [1c] and Shanyong Wang [2d]

[1] *School of Civil Engineering, Chongqing University, Chongqing 400045, China*
[2] *Priority Research Centre for Geotechnical Science and Engineering, School of Engineering, The University of Newcastle, Callaghan, NSW, 2308, Australia*

(*Received January 20, 2022, Revised June 21, 2022, Accepted July 6, 2022*)

Abstract. In this paper, a new sensor chip with frequency reconstruction range of 2.252 GHz ~ 2.450 GHz is designed and fabricated. On this basis, a self-designed "T-shaped" shell is added to overcome the disadvantage of uneven deformation of the traditional steel shell, and the range of the sensor chip is expanded to 0 kN ~ 96 kN. The liquid metal antenna is used to carry out a step-by-step loading test, and the relationship between the antenna resonance frequency and the pressure load is analyzed. The results show that there is a good linear relationship between the pressure load and the resonant frequency. Therefore, the liquid metal antenna can be regarded as a pressure sensor. The cyclic loading and unloading experiments of the sensor are carried out, and different loading rates are used to explore the influence on the performance of the sensor. The loading and unloading characteristic curves and the influence characteristic curves of loading rate are plotted. The experimental results show that the sensor has no residual deformation during the cycle of loading and unloading. Moreover, the influence of temperature on the performance of the sensor is studied, and the temperature correction formula is derived.

Keywords: liquid-metal-antenna-based on sensor; polydimethylsiloxane (PDMS); pressure sensor; reconfigurable antenna

1. Introduction

The pressure sensor is a key instrument that can directly obtain the internal stress distribution and magnitude of rocks and soils. Its main working principle is to convert the external pressure signal into an electrical signal according to a certain rule. In a variety of industries, pressure sensors, as the most common sensor type, have received widespread attention. According to the different working principles, pressure sensors are mainly divided into the following categories: resistance strain gauge pressure sensor (Yu *et al*. 2010, Lebedev *et al*. 2012, Zheng *et al*. 2013), piezoresistive sensor (Wang *et al*. 2020, Georgopoulou *et al*. 2021), piezoelectric pressure sensor (Stefan *et al*. 2017, Kim *et al*. 2020), capacitive pressure sensor (Ko 1986, Ko *et al*. 1983), antenna frequency pressure sensor (Wang 2010, Choi *et al*. 2015, Xu *et al*. 2016, Dildar *et al*. 2020, Liu *et al*. 2020, Lee *et al*. 2020, Mathur *et al*. 2020, Saha *et al*. 2020). However, the sensitive elements of traditional sensors used in practical engineering are usually rigid materials, which have the characteristics of low flexibility and high brittleness. As a result, the sensor (Ren *et al*. 2016) is prone to mechanical brittle fracture and fatigue failure under cyclic load. Flexible sensors (Li and Zhang 2008, Chuang *et al*. 2012, Min *et al*. 2019, Zhang 2019, Zhou and Yu 2021) usually refer to sensors made of flexible materials with excellent ductility. Moreover, the structure of the flexible sensor can be changed in many ways, and it can be arbitrarily arranged under different measurement conditions, so that it can monitor the complex engineering environment.

At present, the fabrication of flexible sensors is usually completed by liquid gallium indium alloy and polydimethylsiloxane (PDMS) as substrate. PDMS has good elasticity and excellent ductility, and can effectively overcome mechanical damage and fatigue damage. For Example, Park *et al*. (2010) prepared a super-elastic pressure sensor by etching gallium-indium microchannels in silicon rubber, which has a resistance change of up to 50% in the pressure range of 0-100 kPa, and these experimental measurements are in good agreement with the theoretical values derived from plane strain elasticity and contact mechanics. In 2012, in order to improve sensitivity and reduce sensor nonlinearity and hysteresis, Park *et al*. (2012a) compared the electrical responses of different cross-sectional geometries and found that channels with triangular or concave cross-sections exhibited minimal nonlinearity and hysteresis. In the same year, a sensor that can detect multiaxial strain and contact pressure was developed, and it can still work under 250% large strains. In 2015, Jung *et al*. (Jung and Yang 2015) successfully introduced this technology into fluid viscosity measurement, which overcomes the complexity of the electrical measurement method and other problems, and its normalized difference is less than 5.1% compared with commercial viscometer evaluation. Zhou *et al*. (2018) developed a three-layer hyper-elastic pressure sensor in

*Corresponding author, Ph.D., Professor,
E-mail: xiao_ping_zhou@126.com
[a] M.D. Student, E-mail: 739193676@qq.com
[b] M.D. Student, E-mail: 734695844@qq.com
[c] M.D. Student, E-mail: 597644285@qq.com
[d] Professor, E-mail: shanyong.wang@newcastle.edu.au

ISSN: 1738-1584 (Print), 1738-1991 (Online)

2018, and designed the pressure sensor shell, so that it can be applied in practical engineering. Cohen *et al*. (2012) proposed a highly elastic strain gauge based on capacitive sensing, which has a variability of less than 3% under strains of up to 100% and thousands of cycles of loading. In 2013, Hu *et al*. (2013) developed a dual-purpose flexible capacitive sensor, which has a strain of up to 60% when measuring uniaxial tension and can withstand a lateral pressure of 1kPa-1MPa, showing good linearity. Unlike the previous works, Pignanelli *et al*. (2019) focused on different etching processes and studied the generation methods of surface patterns of four different PDMS media. By comparing with different patterned media, we can understand the influence of flexible microstructure design on pressure sensitivity, which provides a new tool for realizing the pressure sensitivity of flexible polymer sensor.

From the working mechanism, the current flexible pressure sensor can be divided into three types: resistive (Ventrelli *et al*. 2009, Park *et al*. 2010, Park *et al*. 2012a, b, Shi and Cheng 2013, Chossaty *et al*. 2015, Jung and Yang 2015, Jiao *et al*. 2016, Otake and Konishi 2018, Zhou *et al*. 2018, Kim *et al*. 2019, Shou *et al*. 2021), capacitive (Cohen *et al*. 2012, Hu *et al*. 2013, Ali *et al*. 2016, 2019, Won *et al*. 2017, Li *et al*. 2019, 2021, Pignanelli *et al*. 2019) and reconfigurable antenna (Traille *et al*. 2008, Deshmukh *et al*. 2011, Khan *et al*. 2011, Dey *et al*. 2013, 2015, Kim *et al*. 2014, Castorina *et al*. 2016, Su *et al*. 2017, Zhang *et al*. 2017, Saptarshi and Sungjoon 2018, Karthikeyan *et al*. 2019, Zhou *et al*. 2019). Among them, only frequency-reconfigurable antenna sensors can be used wirelessly. Moreover, the eutectic gallium-indium alloy (EGaIn), with liquid fluidity, metal conductivity and a unique self-repairing ability, is suitable for fabricating frequency-reconfigurable antennas. The liquid metal can harmoniously flow with the deformation of PDMS, so the frequency of the antenna is reconfigurable. For example, Traille *et al*. (2008) proposed a novel concept of liquid antenna, which can increase the range of the antenna by 5-10 times by changing the salinity of the liquid antenna, and they envisaged that similar methods can be extended to the development of liquid radio frequency electronics for implantable devices and wearable real-time biological signal monitoring. In 2011, Khan's team (Khan *et al*. 2011) created a liquid metal antenna that can measure the pressure range, but the pressure value cannot be accurately calibrated. Zhou *et al*. (2019) developed a symmetric dipole pressure sensor, and the experimental results show that the linear relationship between displacement and its resonance frequency is in good agreement with the numerical and theoretical calculation results. However, these flexible frequency-reconfigurable antenna sensors generally have the disadvantages of large size and small measuring range.

This paper uses soft lithography technology to etch PDMS into a microfluidic chip as the base material, and encapsulate liquid metal into the microfluidic chip to fabricate a liquid metal antenna as a pressure sensor. This liquid metal sensor antenna adopts the structure of a loop antenna, which breaks through the shortcomings of the traditional symmetrical dipole structure and reduces the overall size of the sensor. In addition, a new type of shell with a "T-shaped" structure is designed and manufactured, which overcomes the shortcomings of the traditional shell's force characteristics and effectively expands the range of the sensor. Due to the high elasticity of the PDMS material and the unique self-healing ability of the liquid metal in the microfluidic channels, the resonant frequency of the liquid metal antenna under pressure is reconfigurable and has certain flexibility characteristics. It can also be combined with radio frequency technology to realize wireless sensing of physical quantities. The sensor is loaded step by step, and the experimental results showed that there is a good linear relationship between the pressure load and the resonance frequency. A cyclic loading and unloading experiments are carried out on the sensor, and the experimental results showed that the repeatability error γ_f and the return error γ_H were ws small, which indicated that the sensor does not produce residual deformation during the cyclic loading and unloading process. In addition, the temperature sensitivity and stability of the sensor are studied. and the temperature correction formula is derived.

2. Sensor design and fabrication

A pressure sensor with a reconfigurable liquid metal antenna is developed, and the antenna is in the form of a loop antenna. The fabrication of the sensor is completed by etching micro flow channels in the PDMS flexible substrate, injecting gallium indium alloy into the channels after the substrate is bonded, encapsulating the liquid injection port and connecting wires, and finally installing the fabricated substrate and shell together.

When the electromagnetic wave propagates in the medium, the expression of the resonant frequency of the antenna is

$$f = \frac{c}{\lambda\sqrt{\varepsilon_{eff}}} \tag{1}$$

where, f is the antenna resonant frequency, λ is the wavelength of the antenna, ε_{eff} is the relative dielectric constant of the medium, and c is the speed of light.

Electromagnetic theory shows that the circumference of the ring antenna is its wavelength when resonance occurs. Eq. (1) shows the theoretical relationship between resonant frequency and antenna size.

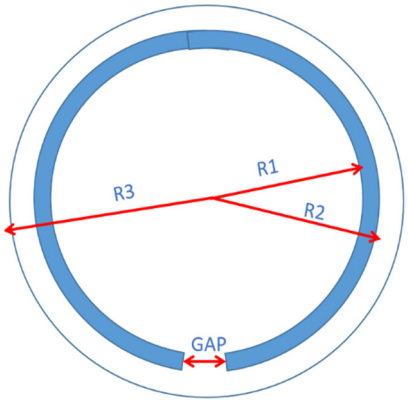

Fig. 1 Planform

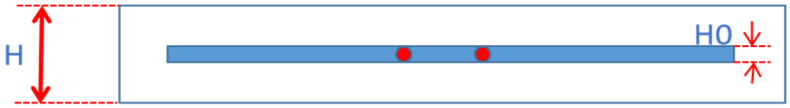

Fig. 2 Side view

2.1 Antenna size determination

In order to facilitate the representation of structural features, the dimensions are shown in Figs. 1 and 2.

In Figs. 1 and 2, the blue represents the micro flow channel encapsulated with liquid metal, and the two red dots in the side view represent the feed of the antenna. R1 is the inner diameter of the liquid metal antenna, R2 is the outer diameter of the liquid metal antenna, R3 is the radius of the entire circular PDMS substrate, GAP is the distance between two feeding points, HO is the height of the micro flow channel, and H is the height of the substrate. Then, HFSS analysis software is used to simulate the influence of parameters on resonant frequency, and the size design of liquid metal antenna is completed.

Firstly, the influence of parameter HO on antenna

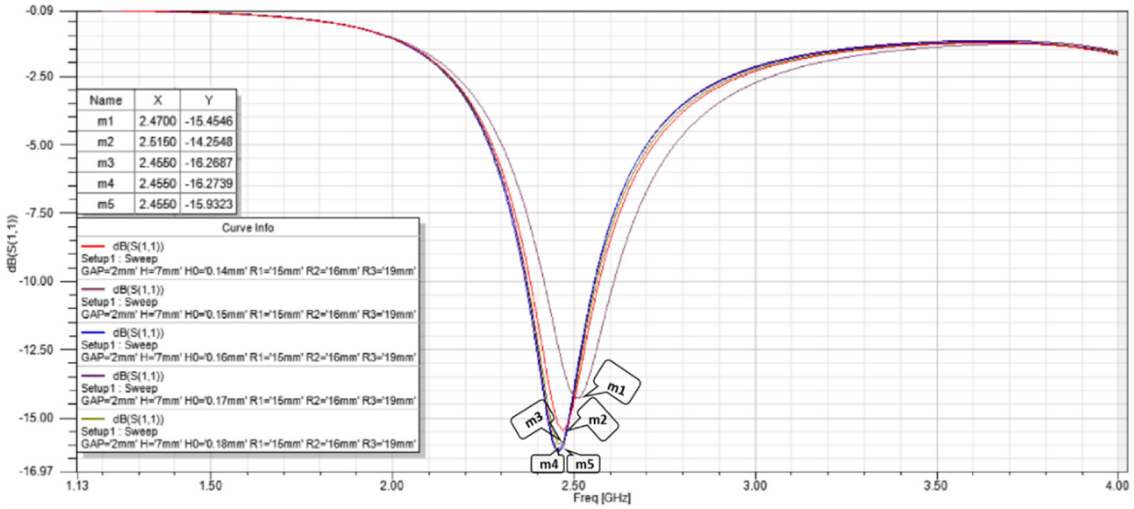

Fig. 3 The effect of parameter HO on the resonant frequency of the antenna

Table 1 Influence of different H0 on resonant frequency

Number	m1	m2	m3	m4	m5
HO/mm	0.14	0.15	0.16	0.17	0.18
f/GHz	2.470	2.515	2.455	2.455	2.455

Table 2 Influence of different R1 on resonant frequency

Number	m1	m2	m3	m4	m5	m6
R1/mm	14.4	14.6	14.8	15.0	15.2	15.4
f/GHz	2.590	2.530	2.500	2.455	2.425	2.395

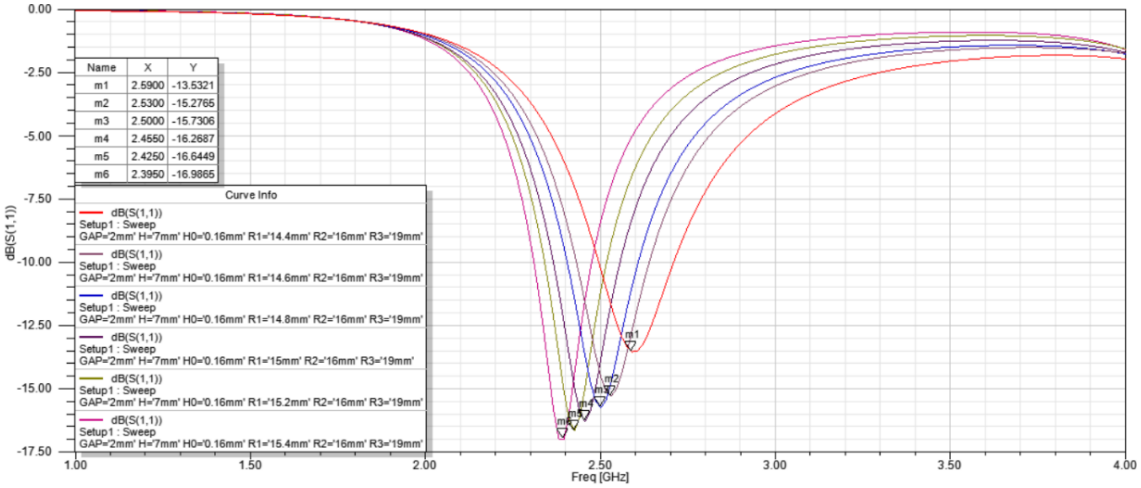

Fig. 4 The effect of parameter R1 on the resonant frequency of the antenna

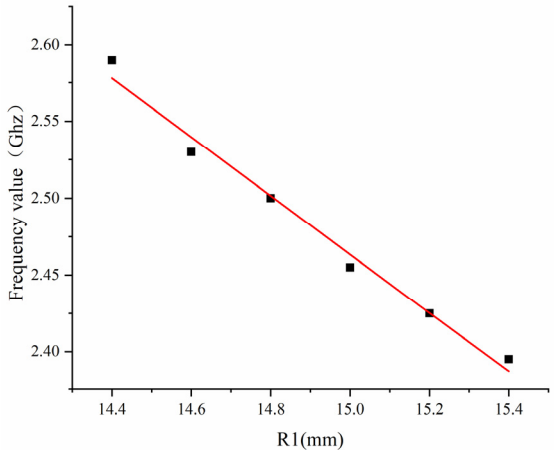

Fig. 5 Linear fitting diagram of R1 and resonant frequency

Table 3 Influence of different R2 on resonant frequency

Number	m1	m2	m3	m4	m5
R2/mm	15.5	16.0	16.5	17.0	17.5
f/GHz	2.425	2.455	2.485	2.515	2.560

resonant frequency is considered, and the simulation results are shown in Fig. 3 and Table 1. It can be seen from Table 1 that there is no obvious corresponding relationship between the section height of liquid antenna and its resonant frequency. Therefore, the value of HO is 0.16 mm.

Based on the above, the influence of parameter R1 (inner diameter) on the resonant frequency of liquid antenna is explored. The results are shown in Fig. 4 and Table 2. It is obvious from Table 2 that the resonant frequency gradually decreases with increasing the radius of the liquid ring antenna. It can be found from Fig. 5 that there exists approximately linear relationship between the resonant frequency and the radius of the liquid ring antenna.

Based on the above, the values of HO and R1 are 0.16 mm and 15 mm, respectively. The influence of R2 (outer diameter) on the resonant frequency of liquid antenna is simulated. The results are shown in Fig. 6 and Table 3. In contrast to R1, the resonant frequency of the liquid antenna is positively correlated with R2. The data are represented by a scatter diagram and are fitted, as shown in Fig. 7. It is found from Fig. 7 that there exists a linear relationship between the resonant frequency and outer diameter.

The resonant frequency designed in this paper is 2.45 GHz and the following parameters are determined from the above analysis: HO = 0.16 mm, R1 = 15 mm, R2 = 16 mm. Then, HFSS is used to simulate the influence of parameter R3 (PDMS chip radius) on the resonant frequency of liquid antenna. The data are shown in Fig. 8 and Table 4. As shown in Fig. 9, the size of R3 has little correlation with the resonant frequency of liquid metal antenna.

In order to ensure that the resonant frequency is 2.45 GHz, the parameters GAP and H are finally determined as 2 mm and 7 mm, respectively. Since these two parameters have little influence on the resonant frequency, the influence of these two parameters is not discussed and studied here. Finally, the simulation results of each data are shown in Fig. 10. At this time, the resonant frequency of the antenna is considered to be 2.45 GHz, and the specific parameters of liquid metal antenna are shown in Table 5.

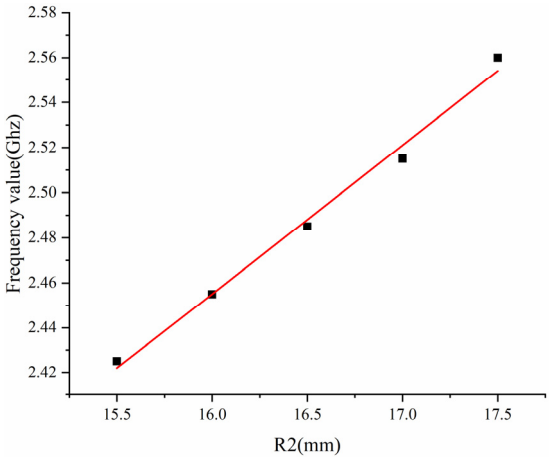

Fig. 7 Linear fitting diagram of R2 and resonant frequency

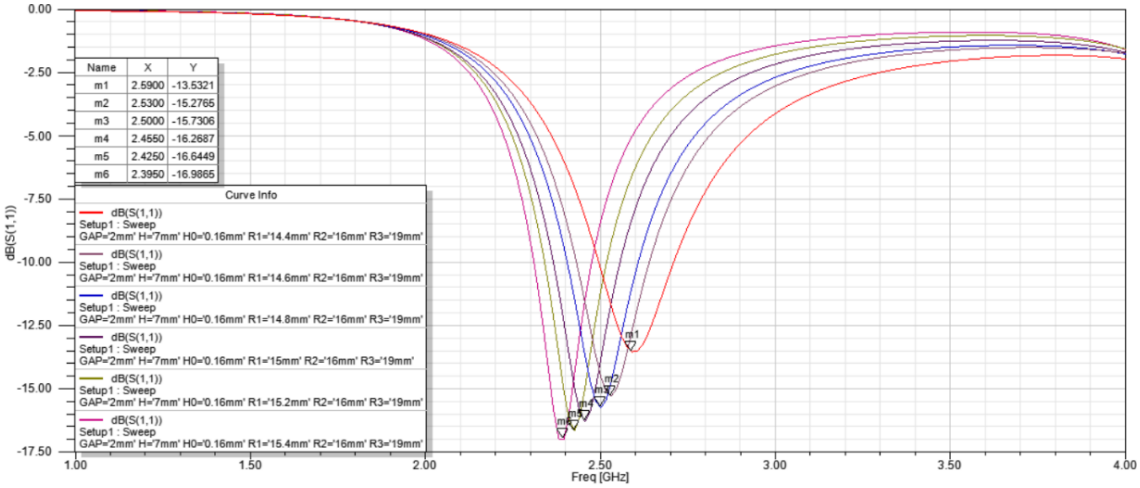

Fig. 6 The effect of parameter R2 on the resonant frequency of the antenna

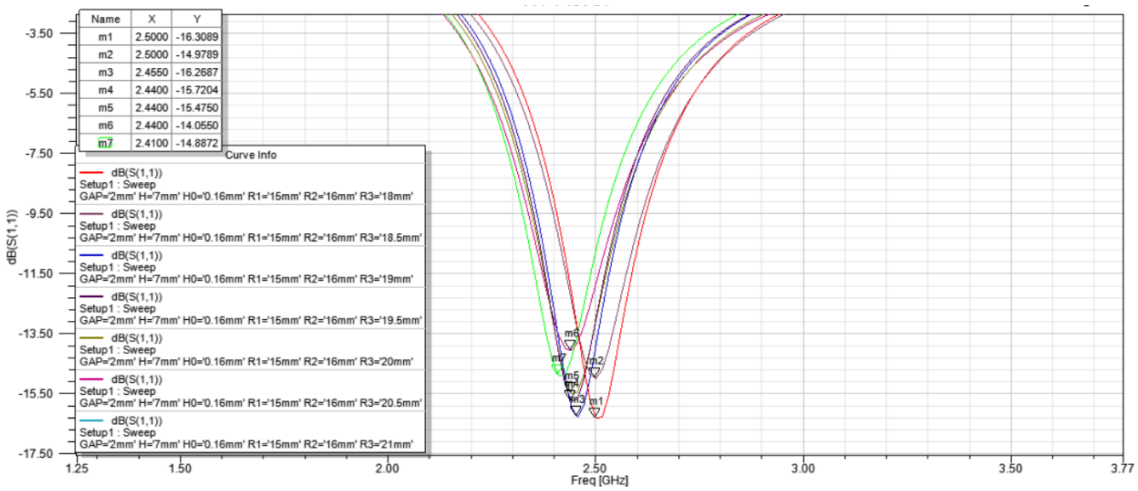

Fig. 8 The effect of parameter R3 on the resonant frequency of the antenna

Table 4 Influence of different R3 on resonant frequency

Number	m1	m2	m3	m4	m5	m6	m6
R3/mm	18.0	18.5	19.0	19.5	20.0	20.5	21.0
f/GHz	2.500	2.500	2.455	2.440	2.440	2.440	2.410

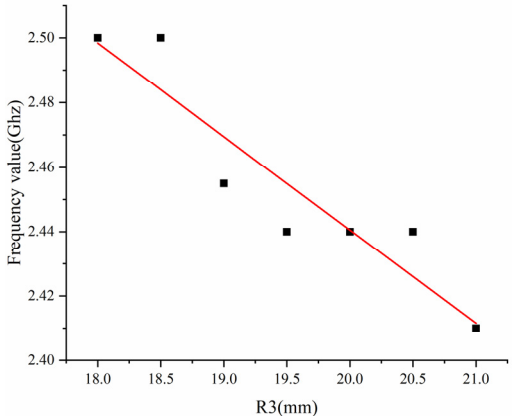

Fig. 9 The relationship between antenna radius R3 and resonant frequency

Table 5 Chip parameters

GAP/mm	H/mm	HO/mm	R1/mm	R2/mm	R3/mm
2	7	0.16	15	16	19

2.2 Manufacturing process

The manufacturing process of antenna is shown in Figs. 11-13, and the process can be divided into the following three steps:

The first step: the mold production of the upper substrate and the lower substrate uses soft lithography technology, and the surface of the mold is processed, as shown in Fig. 11.

The second step: the ratio of polydimethylsiloxane (PDMS) and curing agent is 10:1. After stirring the mixture in a container, it is placed in a vacuum chamber to remove bubbles. The mixed liquid is poured into the mold, and the mold is placed on a heating Table at 80℃ until it is completely solidified. PDMS is released from the mold, and the two ends of the microfluidic channel are punched with a stainless-steel tinned round punch with a size of 0.2 mm ×

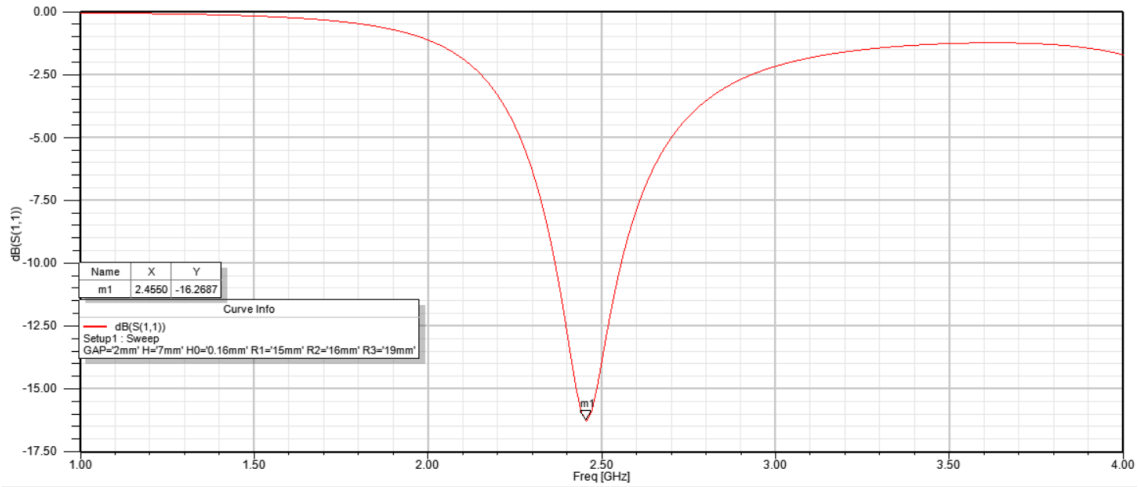

Fig. 10 Final size determination

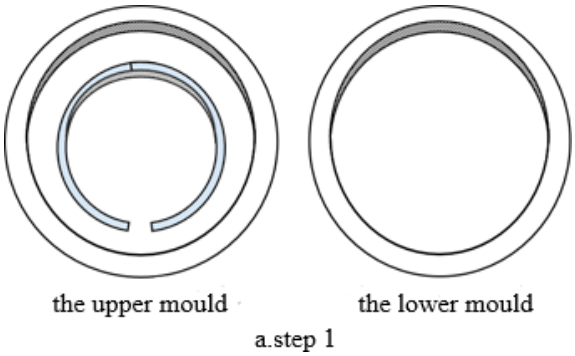

Fig. 11 Mould manufacture

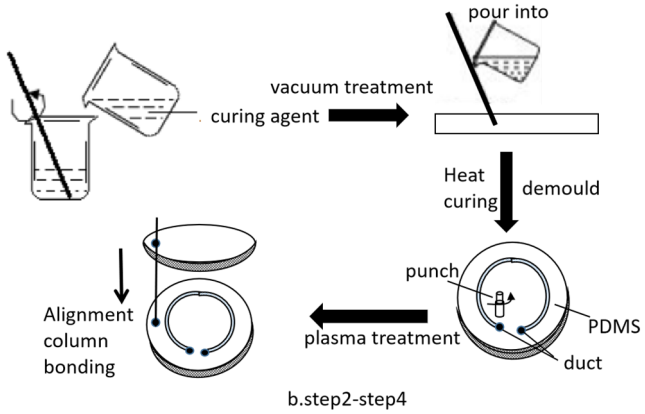

Fig. 12 Demoulding and bonding

1 mm to form a through hole as the main injection port. For precise bonding, the substrates are aligned through the alignment pillars, and then the substrates are bonded by their own gravity after alignment, as shown in Fig. 12.

The third step: After the bonding of the substrate is completed, the liquid metal Galinstan is injected into the micropores through a syringe. The wires at the entrance and exit are connected, and high-viscosity and heat-stable adhesive is used to seal the connection position, as shown in Fig. 13.

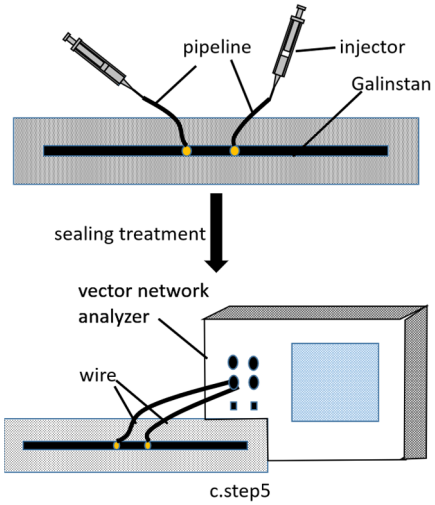

Fig. 13 Made and measured

Fig. 14 The finished PDMS substrate

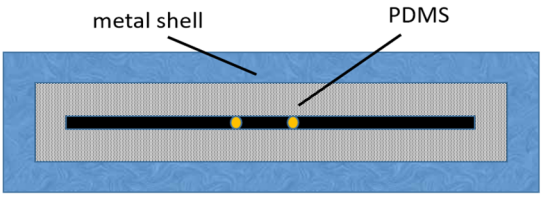

Fig. 15 Conventional shell construction

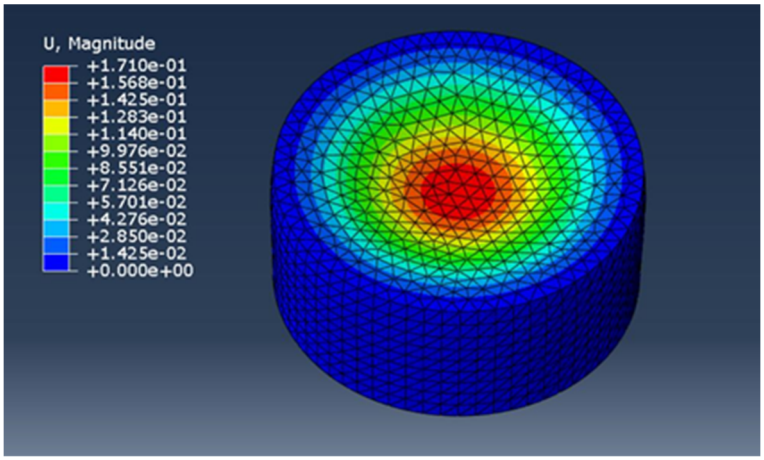

Fig. 16 Cloud image of conventional shell structure under stress and deformation

After the above steps, a reconfigurable liquid metal antenna chip is designed and manufactured, and the finished product is shown in Fig. 14.

2.3 Design of sensor shell

When the shell is under pressure, the surface is deformed. For the conventional shell structure shown in Fig. 15, when it is subjected to pressure, it may produce uneven deflection, a concave three-dimensional curved surface may be formed, leading to non-uniform distribution of the pressure acting on the PDMS chip. To reflect the uneven deformation of the traditional shell, ABAQUS software is used for simulation, and the simulation result is shown in Fig. 16. It can be seen from Fig. 16 that the closer the center part, the greater the deformation. Correspondingly, the contact pressure acting on the internal PDMS chip is not an ideal uniform force. Therefore, in order to solve this problem, the shell needs to be optimized.

In this paper, a new shell is developed, whose internal structure is "inverted T-shaped" pressure structure. Through this structure, the uneven pressure can be converted into uniform equivalent pressure skillfully, as shown in Fig. 17.

Schematic diagram of "inverted T" shell structure is plotted in Fig. 18. To determine the dimensions of "inverted T" shell structure, FEM (Abaqus software) is used to

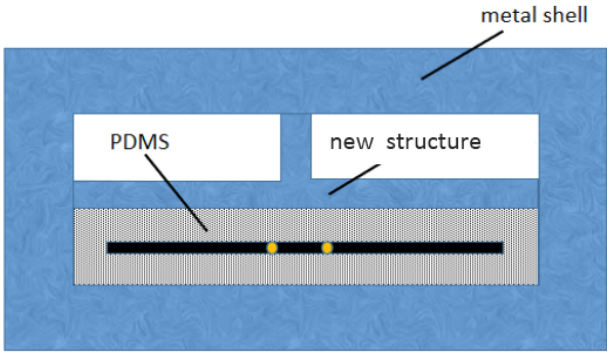

Fig. 17 "Inverted T" shell construction

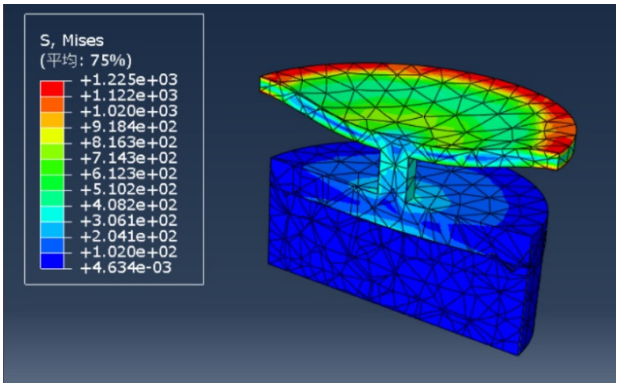

Fig. 19 Schematic diagram of shell internal structure

Fig. 20 The manufactured shell

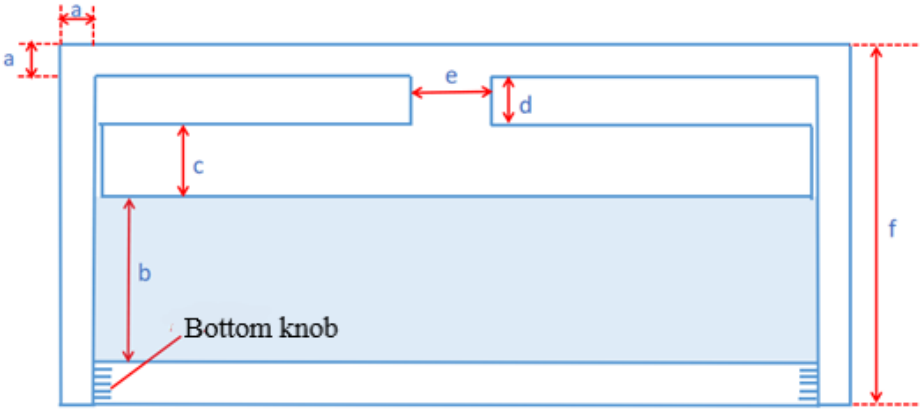

Fig. 18 Schematic diagram of shell internal structure

Table 6 Enclosure parameter value

a	b	c	d	e	f	Shell section (loop)	
						Internal diameter	External diameter
2 mm	7 mm	4 mm	3 mm	4 mm	18 mm	19 mm	21 mm

simulate its deformation. Considering the characteristics of the shell material and practical engineering applications, the stress and vertical deformation under different shell sizes are compared, and a relatively suitable size is determined. The final deformed contour is shown in Fig. 19. It can be seen from Fig. 19 that the color of the stress contour at the bottom tends to be consistent. Therefore, the external pressure can be approximately regarded as uniform pressure through the buffer of the inverted T-shaped structure. Finally, the dimension of the new shell structure is shown in Table 6. The manufactured shell structure is shown in Fig. 20.

3. Theoretical analysis

When theoretical analysis is conducted, some assumptions need to be defined in this paper. The following assumptions are indispensable:

(1) The selected production materials have good elastic properties, such as steel shell and PDMS with internal chip. It is assumed that sensors made of these materials do not produce residual deformation and hysteresis in actual use.
(2) Assuming that the "inverted T-shaped" pressure structure inside the shell is rigid and does not produce any deformation. Its main function is to convert uneven pressure into uniform stress, so that the PDMS chip can be stressed uniformly.
(3) Compared with the elastic modulus of PDMS, the elastic modulus of the shell is several orders of magnitude higher. When external force acts on the sensor, the effects of its deflection and deformation on internal chip does not need to consider.
(4) The premise of the small deflection theoretical analysis of the shell is to satisfy the Kirchhoff hypothesis.

3.1 The deformation of the sensor shell

Different from the traditional shell, the working principle of the sensor of the new shell in this paper is that its deflection deformation induced by external force causes the change of its electrical signal. Therefore, it is necessary to establish the relationship between the external pressure and the deflection change at the center of the metal shell. As shown in Fig. 21, the radius of the circular thin plate is R, the thickness is t, and the uniform load is denoted as P. The coordinate system is a cylindrical coordinate system, and the radial distance, azimuth angle, and height are marked as r, θ, and z, respectively.

Firstly, the equilibrium equation, physical equation and geometric coordination equation are constructed. Considering a micro-element body for moment-equilibrium analysis, we can determine Eq. (2). Considering the distance between the radial section and the midplane as z, the micro-segment is used to analyze the geometric equation, and the geometric equation of the relationship between strain and deflection can be obtained, as shown in Eq. (3). Finally, the physical equation is derived according to the generalized Hooke's law, as shown in Eq. (4).

$$M_r + \frac{dM_r}{dr} - M_\theta + Q_r \mathrm{r} = 0 \tag{2}$$

$$\begin{cases} \varepsilon_r = -\mathrm{z}\dfrac{d^2w}{dr^2} \\ \varepsilon_\theta = -\dfrac{z}{r}\dfrac{dw}{dr} \end{cases} \tag{3}$$

$$\begin{cases} \sigma_r = \dfrac{E}{1-\mu^2}(\varepsilon_r + \mu\varepsilon_\theta) \\ \sigma_\theta = \dfrac{E}{1-\mu^2}(\varepsilon_\theta + \mu\varepsilon_r) \end{cases} \tag{4}$$

where, $M_r$is the radial bending moment of micro element, M_θ is the axial bending moment of micro element, Q_r is the transverse shear force of micro element, z is the distance between the radial section and the midplane, r is the radius, w is the deflection, $\varepsilon_r, \varepsilon_\theta$ are the strains, σ_r, σ_θ are the stresses, E is theYoung's modulus, and μ is the Poisson's ratio.

Combining Eqs. (3) and (4), the relationship between deflection and stress is written as

$$\begin{cases} \sigma_r = -\dfrac{Ez}{1-\mu^2}\left(\dfrac{d^2w}{dr^2} + \dfrac{\mu}{r}\dfrac{dw}{dr}\right) \\ \sigma_\theta = -\dfrac{Ez}{1-\mu^2}\left(\dfrac{1}{r}\dfrac{dw}{dr} + \mu\dfrac{d^2w}{dr^2}\right) \end{cases} \tag{5}$$

By integrating σ_r and σ_θ, the expressions of M_r and M_θ with deflection are obtained as

$$\begin{cases} M_r = -D'\left(\dfrac{d^2w}{dr^2} + \dfrac{\mu}{r}\dfrac{dw}{dr}\right) \\ M_\theta = -D'\left(\dfrac{1}{r}\dfrac{dw}{dr} + \mu\dfrac{d^2w}{dr^2}\right) \end{cases} \tag{6}$$

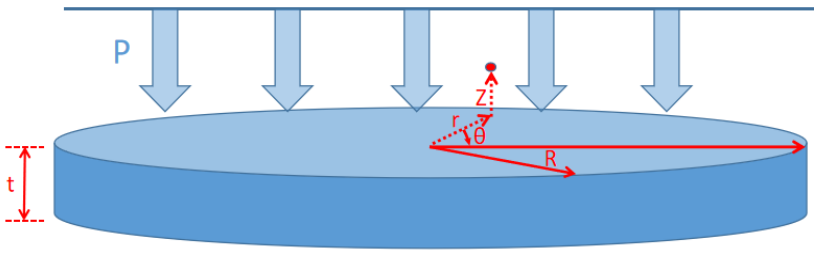

Fig. 21 Schematic diagram of circular thin plate under stress

where, $D' = \frac{Et^3}{12(1-\mu^2)}$ represents the bending stiffness of the circular plate, which is only related to the geometric size and material properties of the circular plate, and t is the thickness of metal shell.

Finally, combining Eq. (6) and Eq. (2), the differential equation for the bending of a circular plate under uniform load is obtained as

$$\frac{d^3w}{dr^3} + \frac{1}{r}\frac{d^2w}{dr^2} - \frac{1}{r^2}\frac{dw}{dr} = \frac{Q_r}{D'} \tag{7}$$

Substituting the expression of Q_r into Eq. (7), the following differential equation can be written as

$$\frac{d}{dr}\left[\frac{1}{r}\frac{d}{dr}\left(r\frac{dw}{dr}\right)\right] = \frac{pr}{2D'} \tag{8}$$

Eq. (8) is integrated three times and can be converted to

$$w = \frac{pr^4}{64D'} + \frac{C_1 r^2}{4} + C_2 Inr + C_3 \tag{9}$$

where, $Q_r = \frac{\pi r^2 p}{2\pi r} = \frac{pr}{2}$, and C_1, C_2, C_3 are integral constants.

According to the boundary conditions, integral constants C_1, C_2 and C_3 can be determined. The deflection w at the center of the plate is a finite value, therefore, the coefficient C_2 is 0. In addition, the boundary condition of the sensor shell is peripheral fixed support, which is written as

$$\begin{cases} w = 0 & r = R \\ \frac{dw}{dr} = 0 & r = R \end{cases} \tag{10}$$

Substituting the above boundary conditions into Eq. (9), the solution of the integral constant is written as

$$\begin{cases} C_1 = \frac{pR^2}{8D'} \\ C_3 = \frac{pR^4}{64D'} \end{cases} \tag{11}$$

Finally, the relationship between the external pressure and the deflection at the center of the metal shell is expressed as

$$w = \frac{pr^4}{64D'} + \frac{C_1 r^2}{4} + C_3 \tag{12}$$

3.2 Theoretical analysis of internal chips

The relationship between the center deflection w of the shell and the vertical strain ε of the chip is written as.

$$\varepsilon = -\frac{w}{H} \tag{13}$$

where, H is the height of the substrate.

The "inverted T-shaped" pressure structure on the upper part of the chip produces the same deflection w as the center of the shell. The lateral strain relation is $\varepsilon_1 = -\mu\varepsilon$ through Hooke's law.

PDMS chip has spatial symmetry on the central axis, which is the same as liquid metal loop antenna. The same spatial symmetry ensures that the shape of the loop antenna remains the loop shape after it is deformed under compression. Based on the elastic assumption mentioned above, the loop antenna can be changed back to its original shape after unloading. This shape design ensures the reconfigurable performance of the antenna sensor.

The relationship between the circumference (L) of the loop antenna and its radius (r') is written as

$$L = 2\pi r' \tag{14}$$

$$r' = (1+\varepsilon_1)\frac{R_1 + R_2}{2} \tag{15}$$

where, L is he circumference of the loop antenna, r' is the radius of the loop antenna, R_1 is the inner diameter of the liquid metal antenna, R_2 is the outer diameter of the liquid metal antenna, and ε_1 is the lateral strain.

Combining the above equation, the relationship between the antenna resonant frequency and the lateral strain ε_1 is expressed as

$$f = \frac{C}{\lambda\sqrt{\varepsilon_{eff}}} = \frac{C}{\pi(1+\varepsilon_1)(R_1+R_2)\sqrt{\varepsilon_{eff}}} \tag{16}$$

where, λ is the antenna wavelength, C is the speed of light, and ε_{eff} is the dielectric constant.

Finally, the theoretical relationship between the deflection w of the center of the shell and the resonance frequency f of the liquid metal antenna in the chip is

$$f = \frac{C}{\lambda\sqrt{\varepsilon_{eff}}} = \frac{CH}{\pi(H + wv)(R_1+R_2)\sqrt{\varepsilon_{eff}}} \tag{17}$$

For this sensor, only the deflection of the center of the circular shell needs to be considered. At this time, the maximum deflection of the center is obtained as

$$w_{max} = \frac{pR^4}{64D'} \tag{18}$$

Combining Eqs. (17) and (18), the final expression between the external pressure p and the signal variable f can be obtained as

$$f = \frac{CH}{\pi(H + \frac{pR^4}{64D'}v)(R_1+R_2)\sqrt{\varepsilon_{eff}}} \tag{19}$$

It can be seen from Eq. (19) that the relationship between the external pressure p and the signal variable presents an inverse proportional function relationship, which can be approximately regarded as a primary function relationship within a certain range.

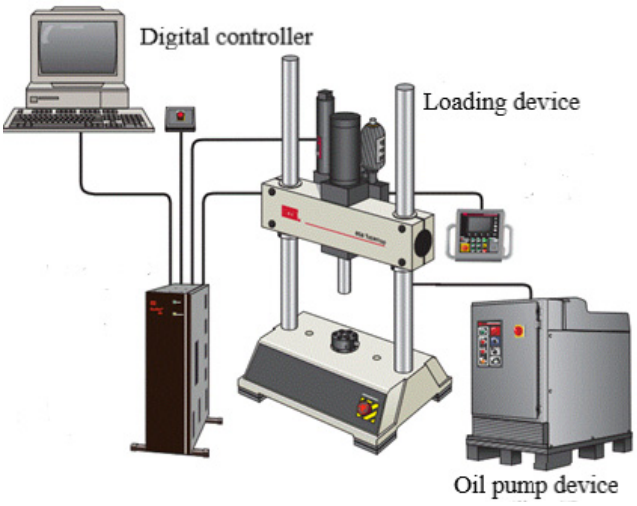

Fig. 22 MTS electro-hydraulic servo test system

Fig. 23 Electronic universal testing machine

4. Test and analysis

4.1 Test equipment

4.1.1 Temperature loading equipment

The MTS electro-hydraulic servo test system can be used for conventional bending and torsion tests of various materials. It can perform tensile, three-point bending test, bending fatigue test, and tensile and compression fatigue test with temperature of various materials. This system is used to test the pressure frequency of the sensor in this paper. In addition, the influence of temperature on the working performance and signal performance of liquid metal antenna sensor is explored. The structure of MTS electro-hydraulic servo test system is shown in Fig. 22.

4.1.2 Cyclic loading equipment

In the pressure-frequency test of the sensor, an electronic universal testing machine is proposed for the pressurized experimental instrument, as shown in Fig. 23. The electronic control system conducts drive control and measures the physical quantities related to force and deformation. Then the computer performs data processing and data analysis, and finally the results are outputted.

Fig. 24 Vector network analyzer (VNA)

4.1.3 Measuring equipment

Vector network analyzer is a common radio frequency measuring instrument, which is mainly used to measure the performance parameters of high-frequency devices, circuits and systems, such as linear parameters, nonlinear parameters, frequency conversion parameters and so on. Considering that the traditional vector network analyzer has the characteristics of large volume, heavy weight and poor movement, a portable vector network analyzer that can meet the accuracy is adopted in the experiment, and its schematic diagram is shown in Fig. 24.

In this experiment, it is planned to apply a maximum load of 96 kN with increasing by 16 kN in each time step, and it holds for 30 s to measure the antenna frequency. Moreover, two samples are set for each group.

4.2 Data analysis

4.2.1 Measured results

The measured frequency values f_1 and f_2 of two identical sensors during the pressure loading process are shown in Table 7.

4.2.2 Theoretical results

The theoretical results of the sensor frequency are shown in Table 8.

Table 7 Measured results

Load F/kN	Measured frequency value(f_1)	Measured frequency value(f_2)
0 kN	2.432 GHz	2.422 GHz
16 kN	2.416 GHz	2.409 GHz
32 kN	2.383 GHz	2.378 GHz
48 kN	2.351 GHz	2.362 GHz
64 kN	2.327 GHz	2.338 GHz
80 kN	2.291 GHz	2.302 GHz
96 kN	2.252 GHz	2.263 GHz

Table 8 Theoretical calculation results

Load F/kN	Deflection of shell center /mm	Theoretical frequency value (f_3)
0 kN	0.000	2.450 GHz
16 kN	0.175	2.420 GHz
32 kN	0.351	2.391 GHz
48 kN	0.526	2.362 GHz
64 kN	0.702	2.334 GHz
80 kN	0.877	2.306 GHz
96 kN	1.053	2.279 GHz

Table 9 Simulation results

Load F/kN	R1/R2 (mm)	Simulated frequency value (f_4)
0 kN	15.000/16.000	2.455 GHz
16 kN	15.188/16.200	2.470 GHz
32 kN	15.375/16.400	2.440 GHz
48 kN	15.563/16.600	2.395 GHz
64 kN	15.750/16.800	2.380 GHz
80 kN	15.938/17.000	2.395 GHz
96 kN	16.125/17.200	2.365 GHz

4.2.3 HFSS software simulation results

In order to compare with the theoretical calculation and actual measurement results, only the inner diameter value R_1 and the outer diameter value R_2 are changed without considering factors such as parameter H. The simulation results are shown in Table 9.

4.2.4 Comparative analysis

The experimental, theoretical, and simulation results of the sensor frequency under pressure are compared, as shown in Figs. 25 to 29. It can be seen from Figs. 25 to 29 that the overall change trend is consistent, except for the

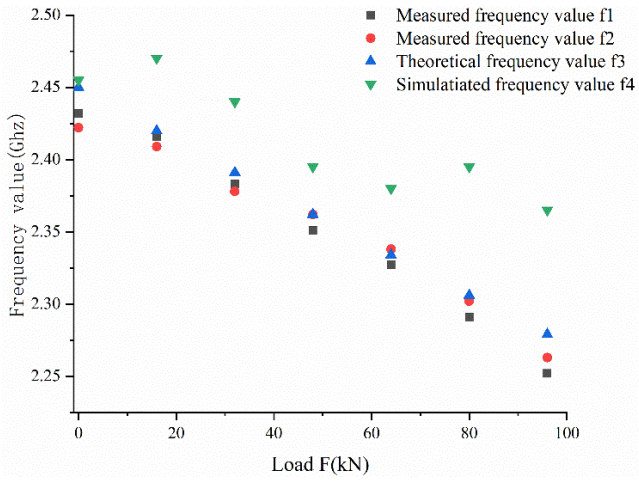

Fig. 25 Scatter diagram of frequency and pressure relationship

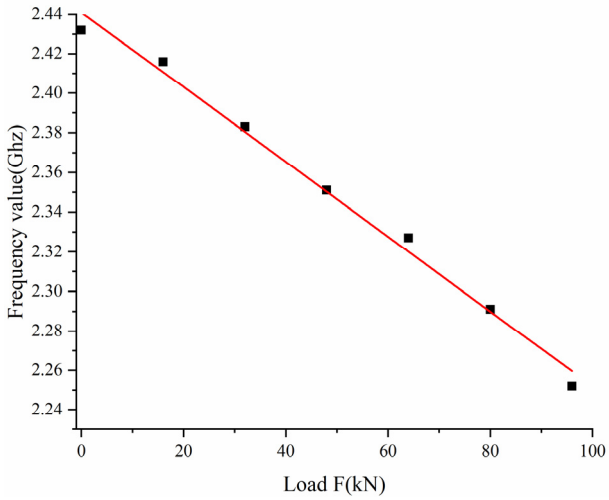

Fig. 26 Diagram of load and theoretical frequency f_1

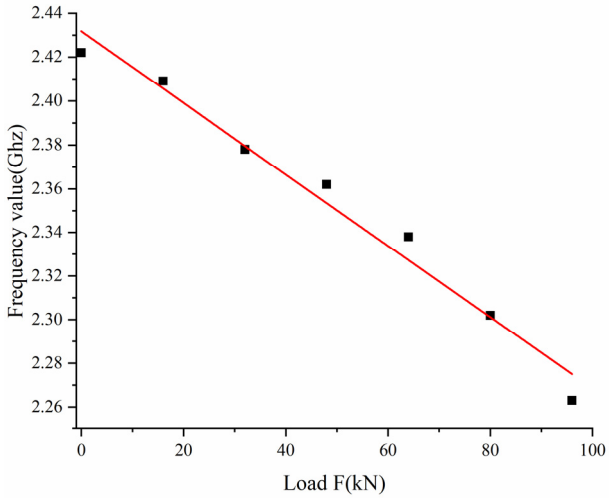

Fig. 27 Diagram of load and theoretical frequency f_2

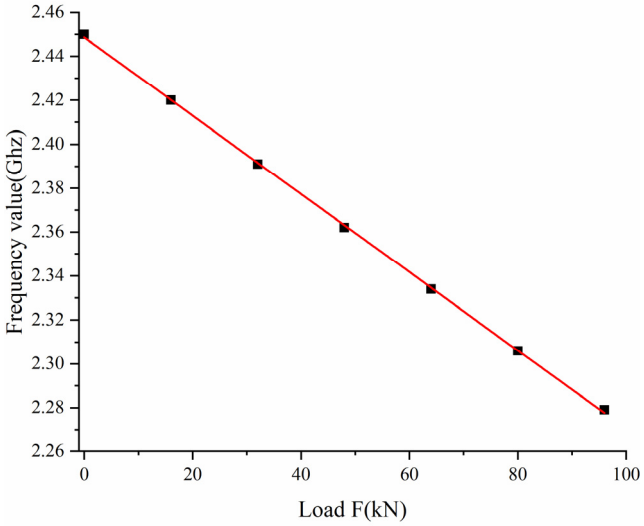

Fig. 28 Diagram of load and theoretical frequency f_3

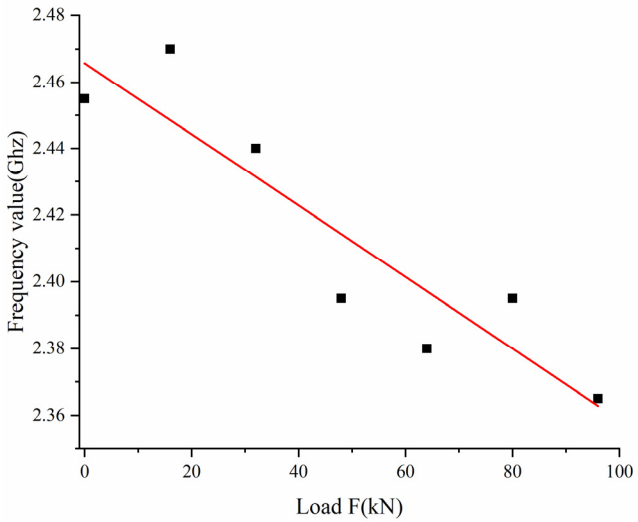

Fig. 29 Diagram of load and theoretical frequency f_4

individual parts of the simulated frequency value f_4. From the numerical point of view, the measured frequency value f_1 and the measured frequency value f_2 are in good agreement with the theoretical frequency value f_3, implying an obvious linear relationship.

Table 10 The fitted parameters

	Measured frequency value (f_1)	Measured frequency value (f_2)	Theoretical frequency value (f_3)	Simulated frequency value (f_4)
A	2.44093	2.43175	2.44864	2.46571
B	-0.00189	-0.00163	-0.00178	-0.00107
R^2	0.99138	0.97729	0.99987	0.84211

Substituting the fitting parameters into the linear relationship $y = A + Bx$, f_1, f_2, f_3, and f_4 are written as Eq. (20). The fitting parameters and results are shown in Table 10.

$$\begin{cases} y_1 = 2.44093 - 0.00189\text{x} \\ y_2 = 2.43175 - 0.00163\text{x} \\ y_3 = 2.44864 - 0.00178\text{x} \\ y_4 = 2.46571 - 0.00107\text{x} \end{cases} \tag{20}$$

where, x represents the pressure load F, y_1 is the measured frequency value, y_2 is the measured frequency value, y_3 is the theoretical frequency value, and y_4 is the simulated frequency value.

The theoretical frequency value y_3 has the best degree of fitness, and R^2 reaches 0.99987. The measured

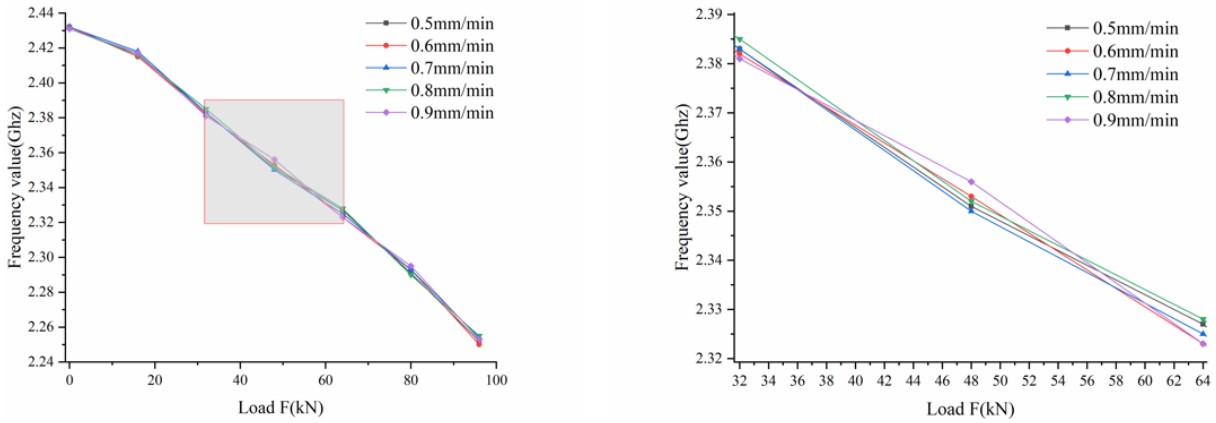

Fig. 30 Frequency - pressure characteristic curves at five different loading rates

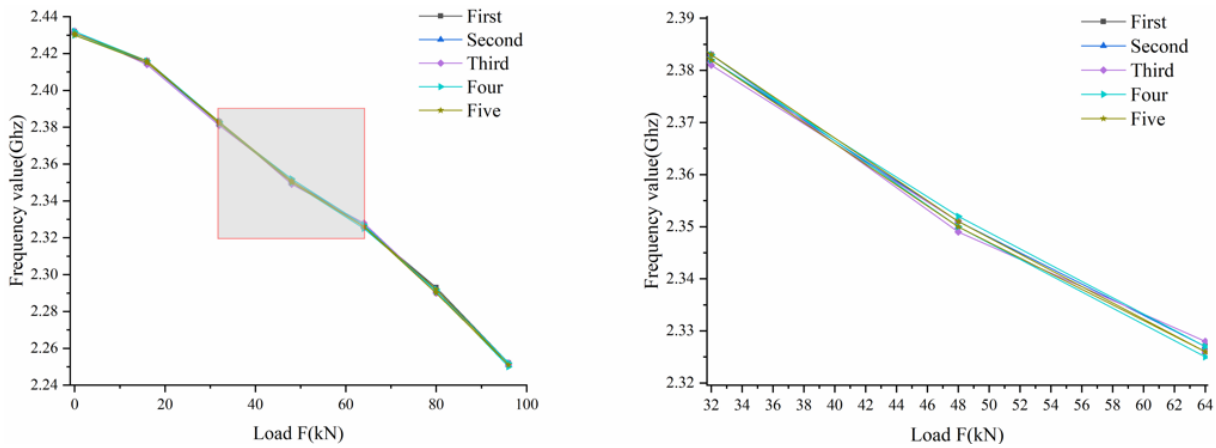

Fig. 31 Frequency - pressure characteristic curves of five cycles loading and unloading

frequency value y_1 and the measured frequency value y_2 also have a good degree of fitness, and they are close in value. However, the fitting of the simulated frequency value f_4 is not ideal, which should be caused by the simulation error only considering the variation of R_1 and R_2 during the simulation.

5. Discussion

5.1 Effect of loading rate

In order to study the effect of loading rate on the performance of the sensor proposed in this paper, uniaxial compression experiments with different loading rates are performed on the sensor samples. The displacement loading rate is set to 0.5 mm/min, 0.6 mm/min, 0.7 mm/min, 0.8 mm/min, 0.9 mm/min in sequence. The test results are shown in Fig. 30. It can be seen from Fig. 30 that the loading rate has a light effect on the characteristic curve of the sensor. Theoretically, the loading rate does not affect the stress-strain curve when the spring steel shell is loaded in the elastic stage. That is to say, whether 0.5 mm/min or 0.9 mm/min is used in the experiment process, when the pressure load reaches the same value, the deformation of the sensor is the same, and the electrical signal output by the corresponding sensor must be the same. From the point of view, the five characteristic lines are relatively close. Considering the experimental error and measurement error, it can be considered that the loading rate has basically no effect on the performance of the sensor.

5.2 Influence of cyclic load

In actual use, the load received by the sensor is cyclic. Under this cyclic load, the sensor may have a certain degree of hysteresis, which may affect the electrical signal output of the pressure sensor. The sensor sample is subjected to a cyclic uniaxial compression experiment, loaded from 0 kN to 96 kN, and then unloaded to 0 kN step by step, which is considered to have completed a cycle. At the same time, the resonant frequency value outputted by the sensor is recorded. The frequency values corresponding to different cycle times are distinguished by different colors, and the results are shown in Fig. 31.

Repeatability is an index to measure the output stability of sensor. Generally, the ratio of the maximum deviation in the same direction of the measurement curve to the full-scale output is regarded as the repeatability error, and its expression is

$$\gamma_f = \left|\frac{\Delta_{fmax}}{y_{Fs}}\right| \times 100\% \tag{21}$$

where, γ_f is the repeatability error, Δ_{fmax} is the maximum deviation in the same direction of the measurement curve, and y_{Fs} is the full-scale output.

The maximum deviation between the measured curves occurs between the third and fourth cycle characteristic curves, and the repeatability error is 1.75%. Because the repeatability error is very small, it can be concluded that there is basically no residual strain after unloading in the above experimental process. This phenomenon coincides with the first assumption of the theoretical analysis, and ensures the basis of the frequency reconfigurable characteristics of the sensor.

Table 11 Antenna starting frequency at different temperatures

10℃ (Room temperature)	2.432 GHz
40℃	2.431 GHz
45℃	2.432 GHz
50℃	2.432 GHz
55℃	2.431 GHz
60℃	2.431 GHz
65℃	2.432 GHz
70℃	2.432 GHz
75℃	2.431 GHz
80℃	2.431 GHz

The phenomenon that the input and output characteristic curves of the sensor subjected to cyclic loading and unloading do not coincide is called hysteresis, which is generally measured by return error, and its expression is

$$\gamma_H = \frac{1}{2}\left|\frac{\Delta_{Hmax}}{y_{Fs}}\right| \times 100\% \tag{22}$$

where, γ_H is the return error, Δ_{Hmax} is the maximum difference of return curve, and y_{Fs} is the the full-scale output.

The repeatability error and return error are 1.75% and 0.58%, respectively. It can be concluded that the sensor has good reusability and measurement accuracy. The sensor basically has no hysteresis, which can be well employed to the cyclic load conditions in the actual use process.

5.3 Temperature influence

5.3.1 Temperature sensitivity analysis

The sensitivity K is calculated by Eq. (23). Firstly, the influence of temperature on the initial frequency of liquid metal antenna is analyzed. The initial frequency of sensor under different temperatures is shown in Table 11. It can be seen from Table 11 that temperature has no obvious effect on the initial resonant frequency because the initial resonant frequency of liquid metal antenna depends on the perimeter embedded in the PDMS chip, and the perimeter is obviously not affected by temperature.

$$K = \frac{\Delta_f}{\Delta_F} \tag{23}$$

where, Δ_f is the change in frequency, and Δ_F is the change in load.

In order to better analyze the impact of temperature on the sensitivity of liquid metal antenna sensor, the initial temperature measurement data are removed here, and the remaining data shown in Fig. 32. It can be seen from Fig. 32 that under the same pressure load, the higher the

Table 12 Fitting curve parameters at different temperatures

	Room temperature (10°C)	40°C	45°C	50°C	55°C	60°C	65°C	70°C	75°C	80°C
A	2.44867	2.45573	2.45427	2.45653	2.45893	2.456	2.43175	2.44864	2.46007	2.46571
B	-0.002	-0.00186	-0.00184	-0.00183	-0.00188	-0.00179	-0.00163	-0.00178	-0.00176	-0.00174
R^2	0.99592	0.99466	0.99296	0.99254	0.99128	0.99363	0.99429	0.991	0.98849	0.98755

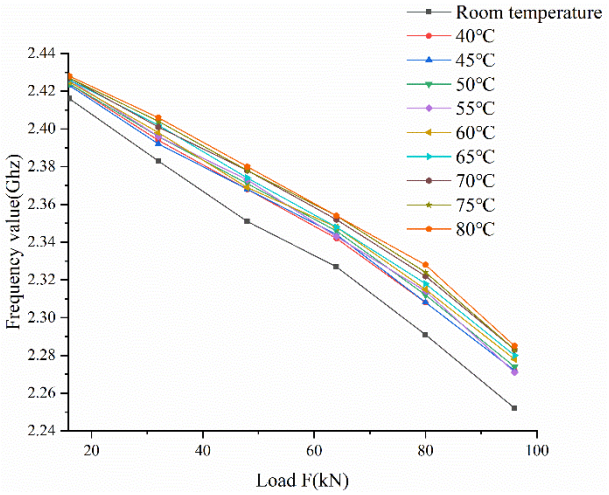

Fig. 32 Performance curve under temperature gradient

temperature, the greater the frequency. In order to deeply study the influence of temperature on the sensitivity of the sensor, the parameters of linear fitting are analyzed. The fitting parameters are shown in Table 12.

It can be found from the Table 12 that the overall trend of sensor sensitivity decreases with the increase of temperature. Numerically, the sensitivity K of the fitting curve of pressure frequency value is 0.002 at room temperature, which is almost 1.12 times that of the fitting curve at 80°C. This change shows that the increase of temperature may lead to the decrease of sensitivity of liquid metal antenna sensor, which is basically consistent with the previous conclusion (Guo *et al*. 2020). The mechanism is that the increase of temperature may change the stress-strain curve of PDMS and its elastic modulus. Then, under the same pressure, the strain of the internal chip becomes smaller, which eventually leads to the smaller slope of the fitting curve and the decrease of the sensitivity of the sensor.

5.3.2 Evaluation of temperature stability

The ratio of the maximum deviation of the experimental data to the full-scale output is proposed to represent its stability, which is recorded as the temperature error, and the expression is written as

$$\gamma = \left|\frac{\Delta_{max}}{y_{Fs}}\right| \times 100\% \tag{24}$$

where, γ is the temperature error, Δ_{max} is the maximum deviation of the experimental data, and y_{Fs} is the full-scale output.

The calculation results of the temperature error at different temperatures are shown in Table 13. When the temperature is lower than 45°C, the temperature error is less than 11.1%, and the maximum temperature error occurs at 80°C, which is equal to 20.6%. This implies that the sensor is suitable for room temperature, and temperature has a greater impact on the performance of the sensor. Therefore, temperature factors must be taken into consideration in actual use.

5.3.3 Derivation of temperature correction

The previous literature shows that the elastic modulus of the spring steel shell (50CrVA) is little affected by temperature, and the initial frequency of the liquid metal antenna is not affected by temperature. Therefore, it can be concluded that the most important influence factor of temperature on the sensor is realized by affecting the elastic modulus of the base material. The relationship between the elastic modulus of the substrate and the temperature is expressed as

$$E_T = E_0 f(\mathrm{T}) \tag{25}$$

where, T represents temperature, E_T and E_0 represent the elastic modulus at temperature T and T_0, respectively.

When the temperature is T, the lateral strain of the chip under the pressure F is expressed as

$$\varepsilon_T = \mu \frac{F}{SE_T} \tag{26}$$

where, μ is the Poisson's ratio of the chip, S is the force area of the chip, and ε_T is the lateral strain of the chip.

When the temperature is T, the frequency f_T of the liquid metal antenna under the pressure F can be expressed as

$$\frac{f_T}{f_0} = \frac{\lambda_o}{\lambda_T} = \frac{R_0}{R_T} = \frac{(1+\varepsilon_0)}{(1+\varepsilon_T)} = f(T)\frac{1+\varepsilon_0}{f(T)+\varepsilon_0} \tag{27}$$

Table 13 Temperature error under different temperature conditions

Temperature	40°C	45°C	50°C	55°C	60°C	65°C	70°C	75°C	80°C
γ	11.1%	11.1%	12.2%	12.8%	14.4%	15.6%	17.2%	18.3%	20.6%

Table 14 Measured results of nylon (GHz)

Temperature \ Load	93 N	186 N	279 N	372 N	465 N	558 N	651 N
10℃	2.412	2.381	2.356	2.324	2.298	2.275	2.256
40℃	2.408	2.372	2.345	2.309	2.275	2.252	2.228
50℃	2.405	2.368	2.338	2.302	2.266	2.238	2.212
60℃	2.403	2.365	2.334	2.291	2.256	2.224	2.202
70℃	2.399	2.359 z	2.326	2.281	2.245	2.210	2.182
80℃	2.398	2.357	2.318	2.272	2.235	2.194	2.167

where $\varepsilon_o = \mu \frac{F}{SE_0}$ represents the lateral strain of the chip when the temperature is T_0 and the pressure load is F, and R_0 and R_T represent the radius of the liquid metal antenna when the temperature is T_0 and T, respectively.

The final expression of f_T is written as

$$f_T = (1 + \varepsilon_0) g(F, T) f_0 \tag{28}$$

$$g(F, T) = \frac{f(T)}{f(T) + \varepsilon_0} \tag{29}$$

Eq. (28) can be used to predict the performance of the sensor at different ambient temperatures, and provides temperature correction.

To verify the applicability of Eq. (28), this paper selects the experimental data, as shown in Table 14.

The relationship of elastic modulus with temperature can be approximately expressed as

$$E_T = 2.934 - 0.014\mathrm{T} \tag{30}$$

where, E_T is elastic modulus of the temperature T.

Finally, the expression of f_T is obtained

$$f_T = f_{10℃} \frac{(1 + 1.357e - 4F)(2.934 - 0.014T)}{2.934 - 0.014T + 3.791e - 4F} \tag{31}$$

Substituting T = 40°C and f_T = 2.345 GHz into Eq. (31), the calculation result of F is 272 N, and the corresponding measured data is 279 N. If temperature correction is not considered, the result of F is 315 N. Therefore, the temperature correction equation is applicable.

6. Conclusions

This paper develops a reconfigurable liquid metal antenna as a flexible pressure sensor, which can overcome the problem of brittle fracture of traditional rigid sensors, and theoretically analyzes the feasibility of the pressure sensor. The resonant frequency range of the sensor varies from 2.252 GHz to 2.450 GHz, and the monitoring pressure range is from 0 kN to 96 kN.

The linear relationship between resonant frequency and pressure is obtained, the relative error of the linearity of the data is very small, and the experimental results are in good agreement with theoretical and simulation data, indicating that the sensor has excellent linearity.

The repeatability error and return error of the proposed sensor are 1.75% and 0.58%, respectively. This implies that the sensor does not produce residual deformation during the cycle of loading and unloading, and it performs well. It can be seen from the experimental results that the loading rate has basically no effect on the working performance of the sensor, because the loading rate does not affect its stress-strain curve in the elastic stage of PDMS. When the pressure is the same value, the deformation of the sensor is the same, the electrical signals outputted by the sensor must be the same.

Temperature has no effect on the initial frequency of the sensor, but has an effect on the sensitivity of the sensor. In general, the higher the temperature, the smaller the slope of its characteristic curve, that is, the worse the sensitivity. In the experimental range, the temperature error of the sensor is 20.56%, so the influence of temperature on the sensor cannot be ignored. This paper derives the temperature correction formula of the sensor, which can predict the influence of temperature factors on the performance of the sensor, thereby improves the reliability of the sensor.

Acknowledgments

The work is supported by the National Natural Science Foundation of China (Nos. 52027814, 51839009).

References

Ali, M.M., Narakathu, B.B., Emamian, S., Chlaihawi, A.A., Aljanabi, F., Maddipatla, D., Bazuin, B.J. and Atashbar, M.Z. (2016), "Eutectic Ga-In liquid metal based flexible capacitive pressure sensor", *Proceedings of IEEE Sensors Conference*, Orlando, FL, USA, October-November. https://doi.org/10.1109/ICSENS.2016.7808515

Ali, S., Maddipatla, D., Narakathu, B.B., Chlaihawi, A.A., Emamian, S., Janabi, F., Bazuin, B.J. and Atashbar, M.Z. (2019), "Flexible capacitive pressure sensor based on PDMS substrate and Ga–In liquid metal", *IEEE Sens. J.*, **19**(1), 97-104. https://doi.org/10.1109/JSEN.2018.2877929

Castorina, G., Donato, L.D., Morabito, A.F., Isernia, T. and Sorbello, G. (2016), "Analysis and design of a concrete embedded antenna for wireless monitoring applications [antenna applications corner]", *IEEE Antennas Propag. Mag.*, **58**(6), 76-93. https://doi.org/10.1109/MAP.2016.2609818

Choi, M., Wi, B., Mun, B., Yoon, Y., Lee, H. and Lee, B. (2015), "A compact frequency reconfigurable antenna for LTE mobile handset applications", *Int. J. Antennas Propag.*, **2015**, 764949.

http://dx.doi.org/10.1155/2015/764949
Chossaty, J.B., Tao, Y., Duchaine, V. and Park, Y.L. (2015), "Wearable soft artificial skin for hand motion detection with embedded microfluidic strain sensing", *Proceedings of IEEE International Conference*, Seattle, WA, USA, July. https://doi.org/10.1109/ICRA.2015.7139544
Chuang, C.H., Liou, Y.R. and Shieh, M.Y. (2012), "Flexible tactile sensor array for foot pressure mapping system in a biped robot", *Smart Struct. Syst.*, *Int. J.*, **9**(6), 535-547. https://doi.org/10.12989/sss.2012.9.6.535
Cohen, D.J., Mitra, D., Peterson, K. and Maharbiz, M.M. (2012), "A highly elastic, capacitive strain gauge based on percolating nanotube networks", *Nano Lett.*, **12**(4), 1821-1825. https://doi.org/10.1021/nl204052z
Deshmukh, S., Xu, X., Mohammad, I. and Huang, H.Y. (2011), "Antenna sensor skin for fatigue crack detection and monitoring", *Smart Struct. Syst.*, *Int. J.*, **8**(1), 93-105. https://doi.org/10.12989/sss.2011.8.1.093
Dey, A., Guldiken, R. and Mumcu, G. (2013), "Wideband frequency tunable liquid metal monopole antenna", *Proceedings of IEEE Antennas and Propagation Society International Symposium* (*APSURSI*), Orlando, FL, USA, July. https://doi.org/10.1109/APS.2013.6710857
Dey, A., Kiourti, A., Mumcu, G. and Volakis, J.L. (2015), "Microfluidically reconFigured frequency tunable dipole antenna", *Proceedings of 9th European Conference*, Lisbon, Portugal, April.
Dildar, H., Althobiani, F., Ahmad, I., Khan, W.U.R., Ullah, S., Mufti, N., Ullah, S., Muhammad, F., Irfan, M. and Glowacz, A. (2020), "Design and experimental analysis of multiband frequency reconfigurable antenna for 5G and sub-6 GHz wireless communication", *Micromachines*, **12**(1), 32. https://doi.org/10.3390/mi12010032
Georgopoulou, A., Michel, S., Vanderborght, B. and Clemens, F. (2021), "Piezoresistive sensor fiber composites based on silicone elastomers for the monitoring of the position of a robot arm", *Sens. Actuator A-Phys.*, **318**, 112433. https://doi.org/10.1016/j.sna.2020.112433
Guo, D.J., Pan, X.D. and He, H. (2020), "Effects of temperature on MWCNTs/PDMS composites based flexible strain sensors", *J. Cent. South Univ.*, **27**(11), 3202-3212. https://doi.org/10.1007/s11771-020-4540-6
Hu, W., Niu, X., Zhao, R. and Pei, Q. (2013), "Elastomeric transparent capacitive sensors based on an interpenetrating composite of silver nanowires and polyurethane", *Appl. Phys. Lett.*, **102**(8), 083303. https://doi.org/10.1063/1.4794143
Jiao, Y., Young, C.W., Yang, S., Oren, S., Ceylan, H., Kim, S., Gopalakrishnan, K., Taylor, P.C. and Liang, D. (2016), "Wearable graphene sensors with microfluidic liquid metal wiring for structural health monitoring and human body motion sensing", *IEEE Sens. J.*, **16**(22), 7870-7875. https://doi.org/10.1109/JSEN.2016.2608330
Jung, T. and Yang, S. (2015), "Highly stable liquid metal-based pressure sensor integrated with a microfluidic channel", *Sensors*, **15**(5), 11823-11835. https://doi.org/10.3390/s150511823
Karthikeyan, M., Park, J. and Lee, D.W. (2019), "Liquid metal based flexible microfluidic device for wireless sensor applications", *Proceedings of 2019 International Conference*, Daejeon, Korea, July. https://doi.org/10.1109/OMN.2019.8925030
Khan, M.R., Hayes, G.J., So, J.H., Lazzi, G. and Dickey, M.D. (2011), "A frequency shifting liquid metal antenna with pressure responsiveness", *Appl. Phys. Lett.*, **99**(1), 013501. https://doi.org/10.1063/1.3603961
Kim, D., Pierce, R.G., Henderson, R., Doo, S.J., Yoo, K. and Lee, J.B. (2014), "Liquid metal actuation-based reversible frequency tunable monopole antenna", *Appl. Phys. Lett.*, **105**(23), 234104. https://doi.org/10.1063/1.4903882
Kim, K., Choi, J., Jeong, Y., Kim, M. Cho, I, Kim, S., Oh, Y. and Park, I. (2019), "Strain-insensitive soft pressure sensor for health monitoring application using 3D-printed microcgannel mold and liquid metal", Pr*oceedings of 20th International Conference*, Berlin, Germany, June. https://doi.org/10.1109/TRANSDUCERS.2019.8808472
Kim, N., Chang, Y.L., Chen, J., Barbee, T., Wang, W., Kim, J.Y., Kwon, M.K., Shervin, S., Moradnia, M., Pouladi, S., Khatiwada, D., Selvamanickam, V. and Ryou, J.H. (2020), "Piezoelectric pressure sensor based on flexible gallium nitride thin film for harsh-environment and high-temperature applications", *Sens. Actuator A-Phys.*, **305**, 111940. https://doi.org/10.1016/j.sna.2020.111940
Ko, W.H. (1986), "Solid-state capacitive pressure transducers", *Sens. Actuator*, **10**(3-4), 303-320. https://doi.org/10.1016/0250-6874(86)80052-X
Ko, W.H., Shao, B.X., Fung, C.D., Shen, W.J. and Yeh, G.J. (1983), "Capacitive pressure transducers with integrated circuits", *Sens. Actuator*, **4**, 403-411. https://doi.org/10.1016/0250-6874(83)85051-3
Lebedev, V., Laukhina, E., Laukhin, V., Rovira, C. and Veciana, J. (2012), "Towards Flexible Lightweight Strain Sensors with Low Temperature Coefficient of Resistance", *Procedia Eng.*, **47**, 857-860. https://doi.org/10.1016/j.proeng.2012.09.282
Lee, S., Lee, M. and Lim, S. (2020), "Frequency reconfigurable antenna actuated by three-storey tower kirigami", *Extreme Mech. Lett.*, **39**, 100833. https://doi.org/doi:10.1016/j.eml.2020.100833
Li, X. and Zhang, Y.F. (2008), "Feasibility study of wide-band low-profile ultrasonic sensor with flexible piezoelectric paint", *Smart Struct. Syst.*, *Int. J.*, **4**(5), 565-582. https://doi.org/10.12989/sss.2008.4.5.565
Li, K., Turcotte, K. and Veres, T. (2019), "Stretchable Strain Sensors based on Thermoplastic Elastomer Microfluidics Embedded with Liquid Metal", *Proceedings of IEEE Sensors Conference*, Montreal, Canada, July. https://doi.org/10.1109/SENSORS43011.2019.8956780
Li, R., Zhou, Q., Bi, Y., Cao, S., Xia, X., Yang, A., Li, S. and Xiao, X. (2021), "Research progress of flexible capacitive pressure sensor for sensitivity enhancement approaches", *Sens. Actuator A-Phys.*, **321**, 112425. https://doi.org/10.1016/j.sna.2020.112425
Liu, G.J., Cao, L.P., Wang, L., Liu, X.N., Du, F.J., Li, Y.Y., Liu, Y.L. and Sun, X.B. (2020), "Design of Frequency Reconfigurable Antenna for WLAN/Bluetooth/WiMAX", *J. Phys.: Conf. Ser.*, **1684**(1), 012157. https://doi.org/10.1088/1742-6596/1684/1/012157
Mathur, P., Madanan, G. and Raman, S. (2020), "Mechanically frequency reconfigurable antenna for WSN, WLAN, and LTE 2500 based internet of things applications", *Int. J. RF Microw. Comput-Aid. Eng.*, **31**(2). https://doi.org/10.1002/mmce.22318
Min, S., Asrulnizam, A., Atsunori, M. and Mariatti, M. (2019), "Properties of stretchable and flexible strain sensor based on silver/PDMS nanocomposites", *Mater. Today: Proceedings*, **17**(3), 616-622. https://doi.org/10.1016/j.matpr.2019.06.342
Otake, S. and Konishi, S. (2018), "Integration of flexible strain sensor using liquid metal into soft micro-actuator", *Proceedings of IEEE Micro Electro Mechanical Systems* (*MEMS*), Belfast, UK, April. https://doi.org/10.1109/MEMSYS.2018.8346617
Park, Y.L., Majidi, C., Kramer, R., Bérard, P. and Wood, R. (2010), "Hyperelastic pressure sensing with a liquid-embedded elastomer", *J. Micromech. Microeng.*, **20**(12), 125029. https://doi.org/10.1088/0960-1317/20/12/125029
Park, Y.L., Chen, B.R. and Wood, R.J. (2012a), "Design and fabrication of soft artificial skin using embedded microchannels

and liquid conductors", *IEEE Sens. J.*, **12**(8), 2711-2718. https://doi.org/10.1109/JSEN.2012.2200790

Park, Y.L., Tepayotl-Ramirez, D., Wood, R.J. and Majidi, C. (2012b), "Influence of cross-sectional geometry on the sensitivity and hysteresis of liquid-phase electronic pressure sensors", *Appl. Phys. Lett.*, **101**(19), 191904. https://doi.org/10.1063/1.4767217

Pignanelli, J., Schlingman, K., Carmichael, T.B., Rondeau-Gagné, S. and Ahamed, M.J. (2019), "A comparative analysis of capacitive-based flexible PDMS pressure sensors", *Sens. Actuator A-Phys.*, **285**, 427-436. https://doi.org/10.1016/j.sna.2018.11.014

Ren, G.J., Cai, C.L. and Wang, D.H. (2016), "Pressure sensor displacement analysis and fatigue lifetime prediction", *Environ. Technol.*, **34**(3), 33-36.

Saha, P.B., Ghoshal, D. and Dash, R.K. (2020), "A miniaturized frequency reconfigurable antenna with half-mode CRLH-embedded metamaterial arm", *J. Electromagn. Waves Appl.*, **35**(3), 277-290. https://doi.org/10.1080/09205071.2020.1832587

Saptarshi, G. and Sungjoon, L. (2018), "A multifunctional reconfigurable frequency-selective surface using liquid-metal alloy", *IEEE Trans. Antennas Propag.*, **66**(9), 4953-4957. https://doi.org/10.1109/TAP.2018.2851455

Shi, X. and Cheng, C.H. (2013), "Artificial hair cell sensors using liquid metal alloy as piezoresistors", *Proceedings of the 8th Annual IEEE International Conference*, Suzhou, China, July. https://doi.org/10.1109/NEMS.2013.6559886

Shou, Y.D.; Zhou, X.P.; Chang, Q.P. and Liu, C. (2021), "An innovative liquid metal-based pressure sensor with its application in geotechnical engineering", *Smart Struct. Syst., Int. J.*, **27**(1), 89-99. https://doi.org/10.12989/sss.2021.27.1.089

Stefan, S., Wedler, J., Rhein, S., Schmidt, M., Körner, C., Michaelis A. and Gebhardt S. (2017), "A process chain for integrating piezoelectric transducers into aluminum die castings to generate smart lightweight structures", *Results Phys.*, **7**, 2534-2539. https://doi.org/10.1016/j.rinp.2017.07.034

Su, W., Nauroze, S.A., Ryan, B. and Tentzeris, M.M. (2017), "Novel 3D printed liquid-metal-alloy microfluidics-based zigzag and helical antennas for origami reconfigurable antenna "trees"", *Proceedings of IEEE MTT-S International Microwave Symposium* (*IMS*), Honololu, HI, USA, June. https://doi.org/10.1109/MWSYM.2017.8058933

Traille, A., Yang, L., Rida, A. and Tentzeris, M.M. (2008), "A novel liquid antenna for wearable bio-monitoring applications", *Proceedings of IEEE MTT-S International Microwave Symposium Digest*, Atlanta, GA, USA, June. https://doi.org/10.1109/MWSYM.2008.4632984

Ventrelli, L., Beccai, L., Mattoli, V., Menciassi, A. and Dario, P. (2009), "Development of a stretchable skin-like tactile sensor based on polymeric composites", *Proceedings of IEEE International Conference*, Guilin, China, February. https://doi.org/10.1109/ROBIO.2009.5420644

Wang, B. (2010), "The United States has developed a self-healing liquid metal antenna", *Funct. Mater. Inf.*, **7**(1), 55-56.

Wang, P.S., Liu, Q., Li, X., Zhang, Z.G. and Zheng, D.M. (2020), "Single crystal silicon high temperature piezoresistive pressure sensor", *Inst. Tech. Sens.*, **2**, 1-3.

Won, D.J., Baek, S., Huh, M., Kim, H., Lee, S. and Kim, J. (2017), "Robust capacitive touch sensor using liquid metal droplets with large dynamic range", *Sens. Actuator A-Phys.*, **259**, 105-111. https://doi.org/10.1016/j.sna.2017.03.032

Xu, D.C., Guo, X.H., Tian, X.J., Liu, W. and Guo, Y.H. (2016), "Design of Dual-Band Flexible Antenna for 2.45 GHz and 5.8 GHz", *J. Jilin Univ.* (Science Edition), **54**(6), 1413-1417.

Yu, L.B., Zhao, Z., Fang, Z., Du, L.D. and Ding, G.J. (2010), "Optimization Design of Mental Strain Pressure Sensor Based on MEMS Technology", *Inst. Tech. Sens.*, **10**, 1-3, 7.

Zhang, T. (2019), "Flexible sensor with new materials to achieve high sensitivity and large strain response", *Sens. World*, **25**(03), 40-41.

Zhang, B., Zhang, L., Deng, W., Jin, L., Chun, F., Pan, H., Gu, B., Zhang, H., Lv, Z., Yang, W. and Wang, Z.L. (2017), "Self-powered acceleration sensor based on liquid metal triboelectric nanogenerator for vibration monitoring", *ACS Nano*, **11**(7), 7440-7446. https://doi.org/10.1021/acsnano.7b03818

Zheng, L.X., Li, Z.Q., Song, X.H. and Zhang, X.Y. (2013), "Research on strain resistance effect of smart concrete under triaxial compression", *J. Sichuan Univ.* (Engineering Science Edition), **45**(2), 33-37.

Zhou, X.P. and Yu, Z.H. (2021), "Flexible multimode pressure sensor based on liquid metal", *Smart Struct. Syst., Int. J.*, **28**(6), 839-853. https://doi.org/10.12989/sss.2021.28.6.839

Zhou, X.P., Deng R.S. and Zhu, J.Y. (2018), "Three-layer-stacked pressure sensor with a liquid metal-embedded elastomer", *J. Micromech. Microeng.*, **28**(8), 085020. https://doi.org/10.1088/1361-6439/aac13c

Zhou, X.P., He, Y. and Zeng, J. (2019), "Liquid metal antenna-based pressure sensor", *Smart Mater. Struct.*, **28**(2), 25019. https://doi.org/10.1088/1361-665X/aaf842

HJ